Journal of Luminescence 238 (2021) 118257

Contents lists available at ScienceDirect

Journal of Luminescence

journal homepage: www.elsevier.com/locate/jlumin

The role of Yb^{2+} as a scintillation sensitiser in the near-infrared scintillator $CsBa_2I_5:Sm^{2+}$

Casper van Aarle [a,*], Karl W. Krämer [b], Pieter Dorenbos [a]

[a] Delft University of Technology, Faculty of Applied Sciences, Department of Radiation Science and Technology, Section Luminescence Materials, Mekelweg 15, 2629 JB, Delft, the Netherlands

[b] University of Bern, Department of Chemistry and Biochemistry, Freiestrasse 3, CH-3012, Bern, Switzerland

A B S T R A C T

The feasiblity of using Yb^{2+} as a scintillation sensitiser for $CsBa_2I_5:Sm^{2+}$ near-infrared scintillators has been assessed. $CsBa_2I_5$ samples with concentrations ranging from 0.3% to 2% Yb^{2+} and 0–1% Sm^{2+} have been studied. The scintillation properties have been determined and the dynamics of the scintillation mechanism have been studied through photoluminescence measurements. Radiationless energy transfer between Yb^{2+} ions plays a key role in increasing the ratio between the spin-forbidden and spin-allowed emission with increasing Yb^{2+} concentration in samples where Yb^{2+} is the only dopant. In samples co-doped with Sm^{2+}, the Yb^{2+} $4f^{13}[^2F_{7/2}]5d_1$[LS] and $4f^{13}[^2F_{7/2}]5d_1$[HS] states both serve as donor states for radiationless energy transfer to Sm^{2+} with a rate of energy transfer that is inversely proportional to the luminescence lifetime the respective donor states. At a Sm^{2+} concentration of 1%, 85% of the Yb^{2+} excitations are transferred to Sm^{2+} through radiationless energy transfer. Almost all of the remaining Yb^{2+} emission is reabsorbed by Sm^{2+}, resulting in nearly complete energy transfer.

1. Introduction

In the past two decades, extensive scintillation research has been performed on Ce^{3+} and Eu^{2+}-doped halides [1]. The best energy resolution that has been measured to date is 2.0% and was achieved by Alekhin et al. with $LaBr_3:Ce^{3+},Sr^{2+}$. The energy resolution of $LaBr_3:Ce^{3+},Sr^{2+}$ is almost entirely determined by Poisson statistics in the number of detected photons [2]. Attaining an energy resolution below 2% thus requires a scintillator with a light yield superior to that of $LaBr_3:Ce^{3+}$ (60,000 ph/MeV [3]) paired with a detector with high quantum efficiency. Additionally, the scintillator needs to have a proportional response to different γ-ray energies.

The light yield and proportionality requirements are satisfied by some Eu^{2+}-doped halide scintillators, such as $CsBa_2I_5:Eu^{2+}$ and $SrI_2:Eu^{2+}$. $CsBa_2I_5:Eu^{2+}$ shows an energy resolution of 2.3% [4] with a light yield of 100,000 ph/MeV [5] and $SrI_2:Eu^{2+}$ shows an energy resolution of 2.7% with a light yield of 115,000 ph/MeV [6]. After absorption of a 1 MeV photon, approximately 100,000 electron hole pairs are created in these scintillators [7], indicating that the probability of the creation of an electron hole pair resulting in an excitation of Eu^{2+} is near unity. Despite this great performance, Eu^{2+}-doped scintillators often suffer from self-absorption, making them less suitable in applications where large crystals are required [8–11].

The problem of self-absorption in Eu^{2+} can be circumvented by co-doping these scintillators with Sm^{2+}. Eu^{2+} is then used as a scintillation sensitiser. Excitation energy of Eu^{2+} is transferred to Sm^{2+}, after which Sm^{2+} emission is observed from any of the $4f^55d \rightarrow 4f^6[^7F_J]$ transitions. As absorption only happens from the $4f^6[^7F_0]$ ground state, emissive transitions to the $4f^6[^7F_{1-6}]$ states reduce the probability of self-absorption [1,12]. If excitations from Eu^{2+} are transferred with high efficiency to Sm^{2+}, the characteristic high light yield of Eu^{2+} doped scintillators is retained. The resulting near-infrared emission from Sm^{2+} can be detected by an avalanche photodiode (APD) with an almost 100% quantum efficiency [13]. Using this approach, Wolszczak et al. measured an energy resolution of 3.2% with $CsBa_2I_5:2\%Eu^{2+},1\%Sm^{2+}$ [14].

In this new class of sensitised scintillators, energy transfer is added as an additional step to the scintillation mechanism. Energy transfer can be separated into two distinct mechanisms, radiative energy transfer and radiationless energy transfer. Radiationless energy transfer is described by Förster-Dexter theory. The probability of energy transfer from a sensitiser's donor state to an acceptor state through dipole-dipole interactions can be described by equation (1) [15]:

$$P_{da}(dd) = \frac{3\hbar^4 c^4 Q_a}{4\pi R^6 n^4 \tau_d} \int \frac{f_d(E) F_a(E)}{E^4} dE \quad (1)$$

Here, $\hbar$ is the reduced Planck constant, c is the speed of light in vacuum, n is the host compounds refractive index and E denotes energy.

* Corresponding author.
E-mail address: c.vanaarle@tudelft.nl (C. van Aarle).

https://doi.org/10.1016/j.jlumin.2021.118257
Received 26 February 2021; Received in revised form 31 May 2021; Accepted 1 June 2021
Available online 10 June 2021
0022-2313/© 2021 The Author(s). Published by Elsevier B.V. This is an open access article under the CC BY license (http://creativecommons.org/licenses/by/4.0/).

R is the distance between the sensitiser and acceptor ions. $f_d(E)$ is the spectral shape of the donor state's emission band and $F_a(E)$ is the spectral shape of the acceptor state's absorption band. The integral is only non-zero if part of the donor state's emission band overlaps with the acceptor state's absorption band. Q_a is the integral over energy of the absorption cross section of the acceptor's absorption band and τ_d is the luminescence decay time of the donor state.

The criterium for radiationless energy transfer is the presence of overlap between the sensitiser's emission spectrum and the acceptor's excitation spectrum. When this criterium is met, radiationless energy transfer from the sensitiser to the acceptor competes with luminescence from the sensitiser's donor state. As the probability of radiationless energy transfer scales with R^{-6}, sensitiser ions close to acceptor ions return to the ground state at a higher rate than those further away [16]. This causes the donor decay time profile to become non-exponential, with faster decay at the beginning and gradually converging to the intrinsic luminescence decay time of the donor [17–19].

When the sensitiser's emission spectrum and the acceptor's excitation spectrum overlap, emission from the sensitiser can also be reabsorbed by the acceptor. This is radiative energy transfer. Sm^{2+} doped in $CsBa_2I_5$ strongly absorbs across the entire optical spectrum, making millimeter-sized crystals of $CsBa_2I_5$:2%Eu^{2+},1%Sm^{2+} already completely opaque [14]. Eu^{2+} emission originating from deep inside the sample will be completely reabsorbed by Sm^{2+}. Only Eu^{2+} emission that originates near the edge of the sample can escape it. Radiative energy transfer thus further increases the fraction of excitations that are transferred from Eu^{2+} to Sm^{2+}. $CsBa_2I_5$:2%Eu^{2+},1%Sm^{2+} is transparent in the near-infrared, so the Sm^{2+} emission is able to exit the sample without being reabsorbed.

Recently, Yb^{2+} has gained in interest as an alternative to Eu^{2+}. Yb^{2+} has a higher atomic number and smaller ionic radius than Eu^{2+} [20], which increases the scintillator's stopping power of γ-rays when introduced in high concentrations. Scintillation properties have been reported for Yb^{2+}-doped $CsBa_2I_5$ [21], SrI_2 [21,22], $SrCl_2$ [23], Cs_4CaI_6 and Cs_4SrI_6 [24]. All of these have light yields reported between 40,000 and 60,000 ph/MeV. The best energy resolution of 3.5% has been achieved with Cs_4CaI_6:1%Yb^{2+}.

Owing to its full $4f^{14}$ subshell, Yb^{2+} does not have any 4f-4f transitions. When exciting an electron to the 5d subshell, the spin-orbit interaction of the remaining $4f^{13}$ core causes a splitting of the $4f^{13}5d$ energy level into $4f^{13}[^2F_{7/2}]5d$ and $4f^{13}[^2F_{5/2}]5d$, referred to as the LS-splitting. The $^2F_{5/2}$ level lies at approximately 10,000 cm^{-1} higher energy than the $^2F_{7/2}$ level [25]. Due to the crystal field interaction with the 5d electron, the $4f^{13}[^2F_{7/2}]5d$ and $4f^{13}[^2F_{5/2}]5d$ levels each split into 5 new energy levels, which we label $5d_n$ with n = 1–5. The size and pattern of the crystal field splitting depends on the coordination number, site symmetry and distance to the surrounding ligands [26]. The total crystal field splitting is defined as the energy difference between the $4f^{13}[^2F_J]5d_1$ and the $4f^{13}[^2F_J]5d_5$ levels. The $4f^{13}$ core and 5d electron both have a spin S=1/2, creating an additional splitting into S=1 (high spin [HS]) and S=0 (low spin [LS]) states, which is named the exchange splitting. Each $4f^{13}[^2F_{7/2}]5d_n$[LS] state lies at approximately 2000 cm^{-1} higher energy than the corresponding $4f^{13}[^2F_{7/2}]5d_n$[HS] state [25].

Yb^{2+} emission has been observed from the $4f^{13}[^2F_{7/2}]5d_1$[LS] → $4f^{14}$ and $4f^{13}[^2F_{7/2}]5d_1$[HS] → $4f^{14}$ transitions, which are referred to as the spin-allowed and spin-forbidden emission, respectively. Room temperature decay times reported for the spin-allowed emission lie typically between 0.1 μs and 1 μs. The spin-forbidden emission is several orders of magnitude slower and reported room temperature decay times lie typically between 100 μs and 1000 μs [22,27,28]. These long decay times cause most of the light to be emitted outside the time window of light collection used in γ-ray spectroscopy, thus making it too slow for scintillator applications. Additionally, the ratio between spin-allowed to spin-forbidden emission is found to decrease with increasing Yb^{2+} concentration in $SrCl_2$ [23], Cs_4CaI_6 and Cs_4SrI_6 [24]. This likely prevents the use of dopant concentrations as high as has often found to be optimal for Eu^{2+} doped halides.

It is often observed that with increase of temperature, the intensity of the spin-allowed emission decreases while simultaneously the intensity of the spin-forbidden increases. This has been attributed to multiphonon relaxation from the $4f^{13}[^2F_{7/2}]5d_1$[LS] state to the $4f^{13}[^2F_{7/2}]5d_1$[HS] state [28]. The temperature at which this thermal relaxation process becomes competitive with the spin-allowed emission strongly depends on the type of anion, being approximately 50 K for fluorides, 200 K for chlorides and 400 K for iodides [29].

Fig. 1 shows the vacuum referred binding energy (VRBE) diagram of $CsBa_2I_5$. The arrows indicate the energy of the transitions that have been reported, from left to right: band gap excitation [10], Sm^{2+} $4f^6$ → $4f^5$5d excitation, Sm^{2+} $4f^5$5d → $4f^6$ emission [14], Eu^{2+} $4f^7$ → $4f^6$5d excitation, Eu^{2+} $4f^6$5d → $4f^7$ emission [10], Yb^{2+} spin-allowed excitation band (this work) and Yb^{2+} spin-allowed emission band [21].

In this work the feasibility of using Yb^{2+} as a scintillation sensitiser for $CsBa_2I_5$:Sm^{2+} scintillators is assessed. The goal is to develop a bright near-infrared scintillator with good energy resolution and reduced self-absorption. For this, samples of $CsBa_2I_5$ with Yb^{2+} concentrations from 0.3% to 5% and Sm^{2+} concentrations from 0% to 1% have been studied for temperatures ranging from 10 K to 550 K. X-ray excited emission spectra have been made to confirm whether most emission comes from Sm^{2+}. The light yield and energy resolution have been determined with ^{137}Cs pulse height spectra. The dynamics of the energy transfer process are studied through spectroscopy and photoluminescence decay time profiles of both Yb^{2+} and Sm^{2+} emission. Additionally, the processes affecting the ratio between Yb^{2+} spin-allowed to spin-forbidden emission are further elaborated on.

2. Experimental techniques

$CsBa_2I_5$:Yb^{2+},Sm^{2+} crystals were grown by the vertical Bridgman technique. CsI (5 N, Alfa) was dried in vacuum at 450 °C. BaI_2 was prepared from $BaCO_3$ (4N7, Alfa), HI acid (57% p.a., Merck KGaA) and NH_4I (3 N, Alfa) following the ammonium halide synthetic route. The ternary product was decomposed at 470 °C in vacuum. The obtained

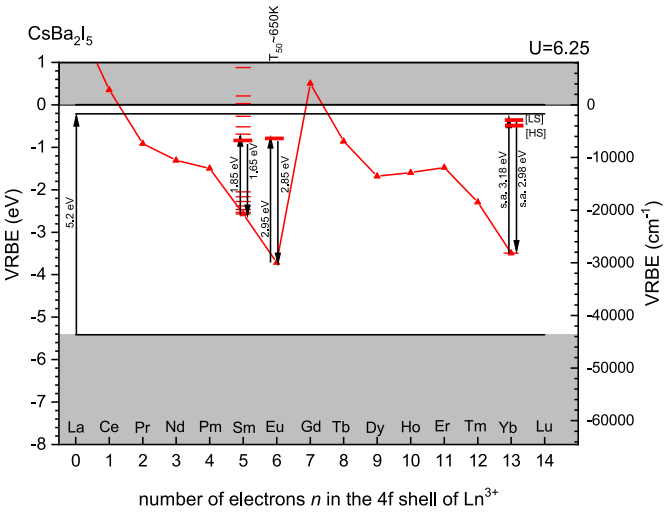

Fig. 1. VRBE diagram of $CsBa_2I_5$, constructed by the method described in Ref. [35]. The parameters used for constructing this diagram are U = 6.25 eV, E_{ex} = 5.2 eV, E_{CT} = 1.7 eV, $\alpha(2+)$ = 0.095, $\beta(2+,A)$ = 0.906 [35]. The U value has been estimated from other iodide compounds [36]. Values for E_{ex}, the Sm^{2+} and Yb^{2+} transitions are presented in this work. The Eu^{2+} transitions have been observed by Alekhin et al. [10].

BaI_2 was purified by melting at 820 °C and crystallization in a glassy carbon ampoule. YbI_2 and SmI_2 were synthesized from the elements (Yb 4 N, Metall Rare Earth Ltd.; Sm 3 N, Alfa; I_2 p.a., Merck KGaA). YbI_2 was prepared from stoichiometric amounts of the elements in a silica ampoule sealed under vacuum. The ampoule was slowly heated to 750 °C in a tube furnace with one end protruding out of the furnace to avoid excessive iodine pressure. YbI_2 was purified by melting at 790 °C and crystallization in a silica ampoule. SmI_3 was prepared from stoichiometric amounts of the elements in a silica ampoule sealed under vacuum. The mixture was heated to 500 °C in a tube furnace, as discussed for YbI_2 above. SmI_3 was purified by sublimation in a silica ampoule at 800 °C under vacuum. SmI_2 was synthesized from SmI_3 and Sm in a tantalum ampoule sealed under vacuum which was heated to 900 °C for one day and 660 °C for three days.

For crystal growth stoichiometric quantities of CsI, BaI_2, YbI_2 and SmI_2 were sealed in a silica ampoule under vacuum and heated to 625 °C, above the congruent melting point of $CsBa_2I_5$ at 610 °C. Crystals were grown by slow cooling with 0.1 mm/min during about ten days. Irregularly shaped crystals of approximately 5 mm in size were cleaved from the boules for spectroscopic investigations. The denoted doping represents the percentage of YbI_2 or SmI_2 replacing BaI_2 in the melt. Since starting materials and products are hygroscopic and sensitive to oxidation, all handling was done under strictly dry and oxygen-free conditions (H_2O and $O_2 < 0.1$ ppm) in glove boxes and sealed sample containers.

Pulse height spectra of $CsBa_2I_5$:0.3%Yb^{2+} and $CsBa_2I_5$:2%Yb^{2+} were measured using a Hamamatsu R6231-100 PMT operated at a voltage of −600 V. The signal from the PMT is amplified by an integrating pre-amplifier followed by an Ortec 672 spectroscopic amplifier, after which the signal is processed by an Ortec 926 analogue to digital converter. The sample was placed on the entrance window of the PMT without optical coupling grease. The scintillator and entrance window were covered with PTFE tape.

Pulse height spectra of $CsBa_2I_5$:2%Yb^{2+},1%Sm^{2+} were measured with an Advanced Photonix APD (type 630-70-72-510) operated at a voltage of 1575 V and at 260 K. The signal from the APD was amplified by a Cremat CR-112 pre-amplifier. The rest of the electronics are the same as used in the PMT set-up described above. The sample was hovering 1 mm above the APD using the pressed powder method described in Ref. [13]. The APD was used without a protective entrance window. For light yield measurements, the location of the photopeak was compared with the peak from direct detection of 17.8 keV X-rays of ^{241}Am.

Photoluminescence emission and excitation spectra were measured using a 450 W Xenon lamp and Horiba Gemini 180 monochromator as excitation source. The emission from the sample passed through an optical filter and Princeton Instruments SpectraPro-SP2358 monochromator before being detected by a Hamamatsu R7600U-20 PMT. The spectra have been corrected for the lamp intensity and the quantum efficiency of the monochromator and PMT.

Photoluminescence decay time profiles have been measured using an EKSPLA NT230 OPO laser as excitation source, with a pulse width of 6 ns and repetition rate of 100 Hz. The emission from the sample passed through an optical filter and Princeton Instruments SpectraPro-SP2358 monochromator before being detected by a Hamamatsu R7600U-20 PMT. The PMT signal was processed using a CAEN DT5730 digitizer.

For all photoluminescence measurements, single crystals of the studied materials were crushed to powder. The hygroscopic material was sealed in gas-tight sample holders with a quartz window. For temperature dependent measurements, the sample holders were mounted on the cold finger of a closed cycle helium cryostat operated at a pressure below 10^{-4} mbar.

X-ray excited emission spectra were measured using an X-ray tube with tungsten anode operated at 80 kV and 1 mm thick copper filter. The emission from the sample passed through a ARC VM504 monochromator before being detected by a Hamamatsu R493-02 PMT. The samples were mounted directly onto the cold finger of a Janis cryostat, which was kept under 10^{-4} mbar during operation.

3. Results

3.1. X-ray excited luminescence and scintillation properties

Fig. 2 shows the X-ray excited emission spectra of (a) $CsBa_2I_5$:0.3% Yb^{2+} and (b) $CsBa_2I_5$:2%Yb^{2+} at 300 K. Both samples show broad asymmetric emission between 20,000 cm^{-1} and 25,000 cm^{-1} (curve 1). This emission has been fitted with two Gaussian functions (dashed curves), revealing two emission bands centered around 22,500 cm^{-1} and 24,000 cm^{-1}. Based on comparison with the $4f^6 5d_1 \rightarrow 4f^7$ emission of $CsBa_2I_5$:Eu^{2+} (23,000 cm^{-1}) [10,30], the emission bands in Fig. 2 are assigned to the spin-allowed $4f^{13}[^2F_{7/2}]5d_1$[LS] → $4f^{14}$ and spin-forbidden $4f^{13}[^2F_{7/2}]5d_1$[HS] → $4f^{14}$ emission. The fit to the spin-allowed emission is narrower than the fit to the spin-forbidden emission. This could in part be due to self-absorption of the spin-allowed emission. Self-absorption makes the spin-allowed emission band narrower and non-Gaussian, but due to the strong overlap between the spin-allowed and spin-forbidden emission bands it is not possible to study their shape in such detail. Despite the difficulty in separating the emission bands, it can be seen that the ratio between the spin-allowed and spin-forbidden emission is higher in $CsBa_2I_5$:0.3%Yb^{2+} than in $CsBa_2I_5$:2%Yb^{2+}. Fig. 2c and d show the X-ray excited emission spectra between 300 K and 450 K. As temperature is increased to 450 K, the intensity of the spin-allowed emission decreases until only spin-forbidden emission is left in both samples.

The X-ray excited emission spectra of $CsBa_2I_5$:2%Yb^{2+},0.5%Sm^{2+}, $CsBa_2I_5$:2%Yb^{2+},1%Sm^{2+} and $CsBa_2I_5$:5%Yb^{2+},1%Sm^{2+} at room temperature are shown in Fig. 3. All the co-doped samples show almost exclusively near-infrared Sm^{2+} emission between 11,000 cm^{-1} and 15,000 cm^{-1}. The same emission was found by Wolszczak et al. in $CsBa_2I_5$:2%Eu^{2+},1%Sm^{2+} and is assigned to the Sm^{2+} $4f^5 5d \rightarrow 4f^6$ transition [14]. The low signal to noise ratio and asymmetry of the emission band is caused by its proximity to the low energy sensitivity edge of the PMT. The emission spectra show no 4f-4f emission lines, which was also observed for $CsBa_2I_5$:2%Eu^{2+},1%Sm^{2+} [14]. The inset shows that a small amount of Yb^{2+} emission can still be detected between 20,000 cm^{-1} and 26,000 cm^{-1}, but no distinction can be made

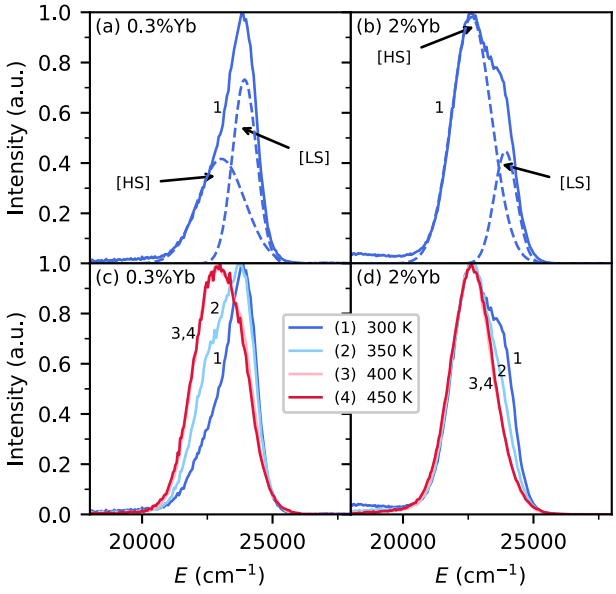

Fig. 2. X-ray excited emission spectra of (a and c) $CsBa_2I_5$:0.3%Yb^{2+} and (b and d) $CsBa_2I_5$:2%Yb^{2+} at 300 K (a and b) and from 300 K to 450 K (c and d).

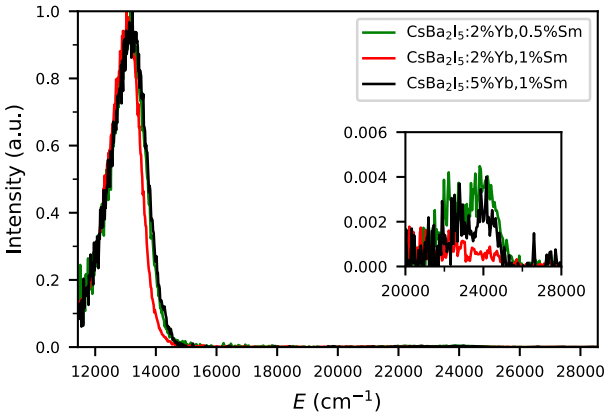

Fig. 3. X-ray excited emission spectra of $CsBa_2I_5$:2%Yb^{2+},0.5%Sm^{2+}, $CsBa_2I_5$:2%Yb^{2+},1%Sm^{2+} and $CsBa_2I_5$:5%Yb^{2+},1%Sm^{2+}. The inset shows an enlarged view of the spectrum between 20,000 cm^{-1} and 28,000 cm^{-1}.

between the spin-allowed and spin-forbidden emission.

Fig. 4a shows the ^{137}Cs pulse height spectrum of $CsBa_2I_5$:0.3%Yb^{2+}. It was measured with a PMT and a shaping time of 10 μs. The light yield has been estimated at 58,000 ph/MeV and an energy resolution of 17.5% was attained. The same PMT and 10 μs shaping time have been used with $CsBa_2I_5$:2%Yb^{2+}, giving a light yield of 39,000 ph/MeV and an energy resolution of 7.2%. About 30% of the light yield is lost when increasing the Yb^{2+} concentration from 0.3% to 2%, although the energy resolution is significantly better.

The pulse height spectrum of $CsBa_2I_5$:2%Yb^{2+},1%Sm^{2+} has been measured using an APD and a shaping time of 10 μs. The light yield has been estimated at 26,000 ph/MeV and an energy resolution of 7,9% was attained. A similar decrease in light yield when co-doping with Sm^{2+} was observed for $CsBa_2I_5$:2%Eu^{2+},1%Sm^{2+} [14]. In attempts to create pulse height spectra with $CsBa_2I_5$:2%Yb^{2+},0.5%Sm^{2+} and $CsBa_2I_5$:5% Yb^{2+},1%Sm^{2+}, no clear photopeak could be observed.

3.2. Spectroscopy

Fig. 5 shows photoluminescence excitation and emission spectra of $CsBa_2I_5$:2%Yb^{2+} at 10 K. The emission spectrum (curve 1) shows the spin-forbidden and spin-allowed emission as two bands of approximately equal intensity at 22,200 cm^{-1} and 24,000 cm^{-1}, respectively. The spin-forbidden and spin-allowed emission bands are well resolved at 10 K. Both emissions show the same excitation bands between 25,000 cm^{-1} and 45,000 cm^{-1} (curves 2 and 3). The excitation spectrum of the spin-forbidden emission (curve 3) shows an additional band at 23,800 cm^{-1}, which is therefore assigned to the spin-forbidden $4f^{14} \rightarrow 4f^{13}[^2F_{7/2}]5d_1$[HS] transition.

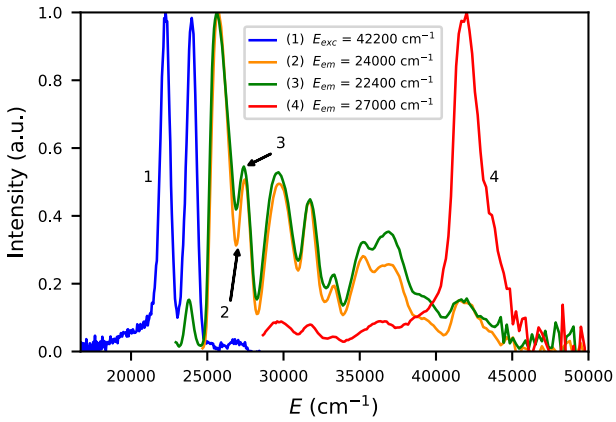

Fig. 5. Photoluminescence excitation and emission spectra of $CsBa_2I_5$:2%Yb^{2+} at 10 K.

The broad emission band between 17,000 cm^{-1} and 21,000 cm^{-1} (curve 1), the emission band at 27,000 cm^{-1} (curve 1) and excitation band at 42,000 cm^{-1} (curve 4) have all been observed in undoped $CsBa_2I_5$. The emission between 17,000 cm^{-1} and 21,000 cm^{-1} was assigned to near-defect exciton emission, the emission band at 27,000 cm^{-1} was ascribed to self-trapped excitons and the excitation band at 42,000 cm^{-1} corresponds to host exciton creation [10]. The latter has been used for constructing the VRBE diagram in Fig. 1.

In Fig. 6, the excitation spectra of the Yb^{2+} spin-allowed and spin-forbidden emission from Fig. 5 are shown together with an Yb^{2+} energy level scheme created from the data. The values for the LS-splitting, crystal field splitting and exchange splitting can be found on the top side of the figure. The energy and transition assignments of the excitation bands are summarised in Table 1.

Band 0 and 1 are assigned to the spin-forbidden $4f^{14} \rightarrow 4f^{13}[^2F_{7/2}]5d_1$[HS] and spin-allowed $4f^{14} \rightarrow 4f^{13}[^2F_{7/2}]5d_1$[LS] transitions, respectively. From this, the value for the exchange splitting of 1900 cm^{-1} is derived, which is in accordance with the typical value of 2000 cm^{-1} for iodide compounds [30,31].

Bands 2 to 5 are assigned to the $4f^{14} \rightarrow 4f^{13}[^2F_{7/2}]5d_{2-5}$[LS] transitions. The transitions to their corresponding [HS] states are not visible in the spectrum due to their lower oscillator strength. The value of the crystal field splitting ε_{cfs} is determined by the difference in energy between band 1 and 5, giving a value of 7600 cm^{-1}. Suta et al. found values of 11,830 cm^{-1} and 10,910 cm^{-1} [31] in $CsCaI_3$:Yb and $CsSrI_3$:Yb, respectively. The approximately equal spacing between bands 1 to 5 suggests that Yb^{2+} is located on a Ba^{2+} site with low symmetry, as a highly symmetric site such as the octahedral coordinated sites in $CsCaI_3$:Yb and $CsSrI_3$:Yb causes the bands to split into two groups, e_g and t_{2g}. Due to the low symmetry of the Ba^{2+} site, the higher coordination

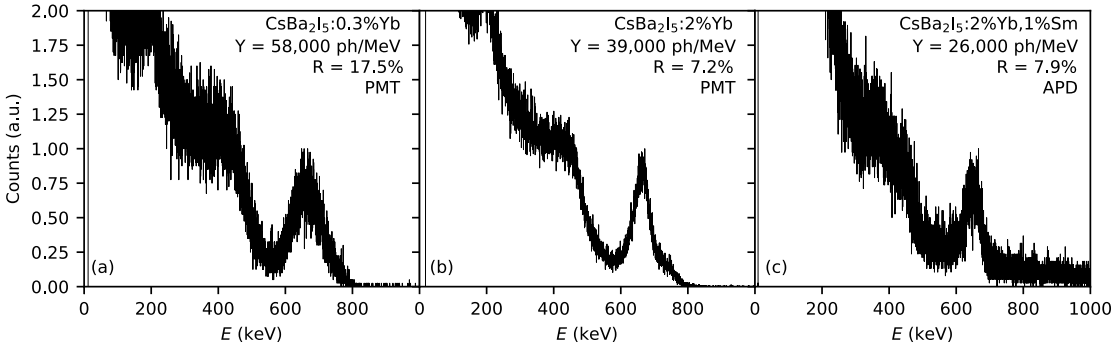

Fig. 4. Pulse height spectra using a ^{137}Cs γ-source. The light yield *Y* and energy resolution *R* of each spectrum are shown as inset. (a) $CsBa_2I_5$:0.3%Yb^{2+} using a PMT as detector, (b) $CsBa_2I_5$:2%Yb^{2+} using a PMT as detector, (c) $CsBa_2I_5$:2%Yb^{2+},1%Sm^{2+} using an APD as detector.

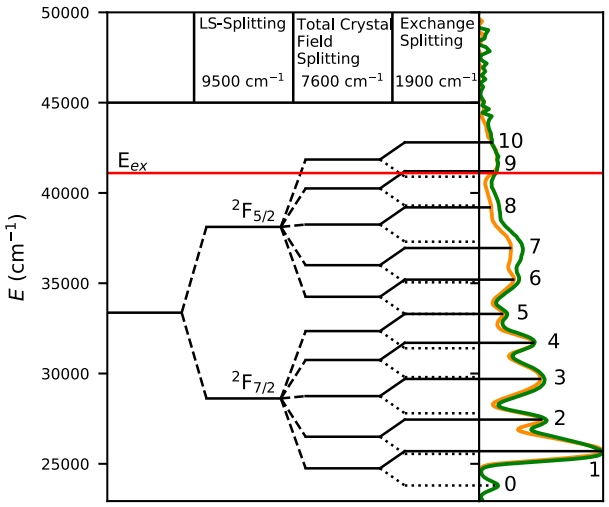

Fig. 6. Energy level scheme of Yb^{2+} in $CsBa_2I_5$ compared to its photoluminescence excitation spectra at 10 K. The leftmost horizontal line corresponds to the value of the $4f^{13}5d$ absorption bands centroid. It is then split up by the LS-splitting into $4f^{13}[^2F_{7/2}]5d$ and $4f^{13}[^2F_{5/2}]5d$ states. These in turn branch out into 5 different states due to the crystal field splitting of the 5d orbitals. Lastly, the scheme is split up by the exchange splitting. The horizontal lines of the energy level scheme are extended to the corresponding peaks in the absorption spectrum. The energy values of the absorption band peaks are listed in Table 1.

Table 1
Energies of the Yb^{2+} excitation bands in $CsBa_2I_5$ measured at 10 K. The numbering of the excitation bands is the same as used in Fig. 6.

#	Transition	Energy (cm^{-1})
0	$4f^{14} \rightarrow 4f^{13}[^2F_{7/2}]5d_1$[HS]	23,800
1	$4f^{14} \rightarrow 4f^{13}[^2F_{7/2}]5d_1$[LS]	25,700
2	$4f^{14} \rightarrow 4f^{13}[^2F_{7/2}]5d_2$[LS]	27,450
3	$4f^{14} \rightarrow 4f^{13}[^2F_{7/2}]5d_3$[LS]	29,700
4	$4f^{14} \rightarrow 4f^{13}[^2F_{7/2}]5d_4$[LS]	31,700
5	$4f^{14} \rightarrow 4f^{13}[^2F_{7/2}]5d_5$[LS]	33,300
6	$4f^{14} \rightarrow 4f^{13}[^2F_{5/2}]5d_1$[LS]	35,200
7	$4f^{14} \rightarrow 4f^{13}[^2F_{5/2}]5d_2$[LS]	36,950
8	$4f^{14} \rightarrow 4f^{13}[^2F_{5/2}]5d_3$[LS]	39,200
9	$4f^{14} \rightarrow 4f^{13}[^2F_{5/2}]5d_4$[LS]	41,200
10	$4f^{14} \rightarrow 4f^{13}[^2F_{5/2}]5d_5$[LS]	42,800

number and the larger ionic radius of Ba^{2+} compared to Ca^{2+} and Sr^{2+} [20], the lower value of 7600 cm^{-1} measured here is expected [26].

Band 6 is assigned to the $4f^{14} \rightarrow 4f^{13}[^2F_{5/2}]5d_1$[LS] transition. The size of the LS-Splitting is determined by the difference between band 1 and band 6, resulting in a value of 9500 cm^{-1}. This is reasonably close to the 10,000 cm^{-1} LS-splitting of the $4f^{13}$ electrons [31,32]. In Fig. 6, the energy of bands 7 to 10 in the energy level scheme are determined by assuming similar crystal field splitting and exchange splitting as observed for the $4f^{13}[^2F_{7/2}]5d_1$ states. This causes accurate alignment with the peaks of bands 7 and 8 in the excitation spectra. Bands 9 and 10 are obscured by the peak corresponding to host exciton creation.

So far, spectroscopic results are given for samples with only Yb^{2+} doping. In samples containing Sm^{2+}, energy transfer is demonstrated when the Yb^{2+} excitation bands appear in the excitation spectrum of Sm^{2+}. Fig. 7 shows photoluminescence excitation and emission spectra of $CsBa_2I_5$:2%Yb^{2+},1%Sm^{2+} at 10 K. Curve 1 shows the emission spectrum at 25,700 cm^{-1} excitation, corresponding to the Yb^{2+} spin-allowed

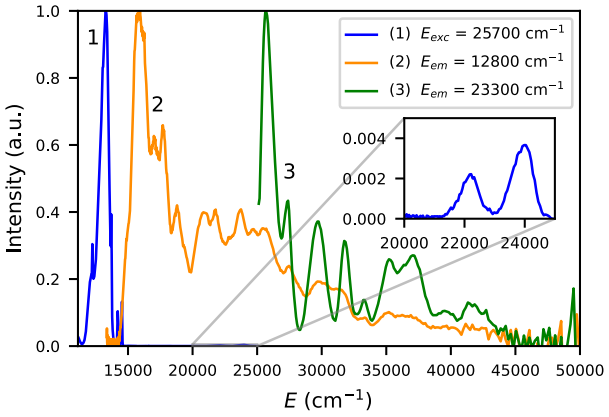

Fig. 7. Photoluminescence excitation and emission spectra of $CsBa_2I_5$:2% Yb^{2+},1%Sm^{2+} at 10 K. The inset shows an enlarged view of the Yb^{2+} emission between 20,000 cm^{-1} and 25,000 cm^{-1}.

$4f^{14} \rightarrow 4f^{13}[^2F_{7/2}]5d_1$[LS] transition. The emission between 12,000 cm^{-1} and 14,000 cm^{-1} is from the Sm^{2+} $4f^55d \rightarrow 4f^6$ transition, as was also observed under X-ray excitation (Fig. 3). Some additional sharp 4f-4f lines are visible at 10 K, but are no longer present at room temperature [33]. The inset shows an enlarged view of the emission between 20,000 cm^{-1} and 25,000 cm^{-1}. The Yb^{2+} spin-forbidden and spin-allowed emission bands can still be observed.

Curve 3 shows the excitation spectrum of the Yb^{2+} emission. The excitation bands are the same as in Fig. 5, indicating that the chemical environment of Yb^{2+} is the same in the Sm^{2+} co-doped sample as in the sample without Sm^{2+}. Curve 2 is the excitation spectrum of the Sm^{2+} emission. It spans across the entire optical spectrum. Between 25,000 cm^{-1} and 40,000 cm^{-1}, the excitation bands of Yb^{2+} are visible in the excitation spectrum, indicating that energy transfer takes place.

3.3. Photoluminescence decay time profiles

Upon excitation at 25,700 cm^{-1}, corresponding to the Yb^{2+} $4f^{14} \rightarrow 4f^{13}[^2F_{7/2}]5d_1$[LS] transition, either spin-allowed emission occurs, or Yb^{2+} relaxes to the $4f^{13}[^2F_{7/2}]5d_1$[HS] state from which the spin-forbidden emission occurs. Additionally, energy can be transferred to Sm^{2+} from both these Yb^{2+} states. 25,700 cm^{-1} photons can also excite Sm^{2+} directly. The dynamics of this system are revealed in the photoluminescence decay time profiles of the Yb^{2+} and Sm^{2+} emissions.

Fig. 8 shows the photoluminescence decay of $CsBa_2I_5$:0.3%Yb^{2+} (curve 1) and $CsBa_2I_5$:2%Yb^{2+} (curve 2) at room temperature. At this temperature, the spin-allowed and spin-forbidden emission bands strongly overlap, causing both emissions to contribute to the decay time profile. The spin-allowed emission decay time is 0.825 μs for $CsBa_2I_5$:0.3%Yb^{2+}. The spin-allowed emission of $CsBa_2I_5$:2%Yb^{2+} is slightly faster and shows noticable non-exponential behaviour.

The spin-forbidden emission decay times are 198 μs and 191 μs for $CsBa_2I_5$:0.3%Yb^{2+} and $CsBa_2I_5$:2%Yb^{2+}, respectively. This part of the decay time profile is almost perfectly exponential in both samples. The ratio between spin-forbidden to spin-allowed emission intensity is higher in $CsBa_2I_5$:2%Yb^{2+} than in $CsBa_2I_5$:0.3%Yb^{2+}, similar to what is found under X-ray excitation (Fig. 2).

In samples co-doped with Sm^{2+}, energy is transferred from Yb^{2+} to Sm^{2+}. Photoluminescence decay time profiles of the Yb^{2+} spin-allowed emission in $CsBa_2I_5$:Yb^{2+},Sm^{2+} are shown in Fig. 9a. Compared to the samples co-doped with Sm^{2+}, $CsBa_2I_5$:2%Yb^{2+} (curve 1) shows almost perfect exponential decay. The Sm^{2+} co-doped samples (curves 2, 3 and 4) show non-exponential decay, indicating that radiationless energy transfer takes place. The rate of energy transfer strongly increases as the Sm^{2+} concentration is increased from 0% (curve 1) to 0.5% (curve 2) to

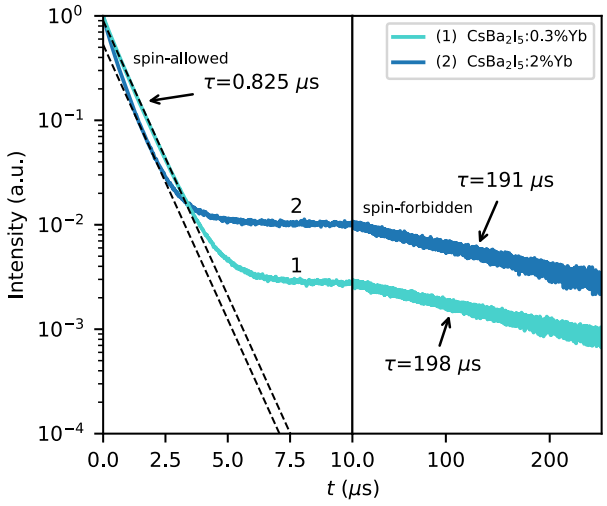

Fig. 8. Photoluminescence decay time profiles of $CsBa_2I_5$:0.3%Yb^{2+} and $CsBa_2I_5$:2%Yb^{2+} excited at 25,700 cm^{-1} and observed at 24,000 cm^{-1} at room temperature. The left and right side of the figure have different time scales.

1% (curve 3), but no significant dependence on the Yb^{2+} concentration is found when comparing $CsBa_2I_5$:2%Yb^{2+},1%Sm^{2+} (curve 3) and $CsBa_2I_5$:5%Yb^{2+},1%Sm^{2+} (curve 4).

For the application as near infra-red scintillator, it is desired that most of the Yb^{2+} excitations are transferred to Sm^{2+}. Radiationless energy transfer competes with Yb^{2+} luminescence. To quantify what fraction of Yb^{2+} excitations is transferred to Sm^{2+} through radiationless energy transfer, the radiationless energy transfer efficiency is estimated using equation (2) [18].

$$\eta_{et} = 1 - \frac{\int_0^\infty \Phi_d(t)dt}{\int_0^\infty \Phi_0(t)dt} \quad (2)$$

Where $\Phi_d(t)$ is the normalised donor decay time profile and $\Phi_0(t)$ is the normalised decay time profile of the donor without any acceptor ions present. The decay time profile of $CsBa_2I_5$:2%Yb^{2+} (Fig. 9a curve 1) has been used as an approximation for $\Phi_0(t)$. The estimated radiationless energy transfer efficiencies are 60% for $CsBa_2I_5$:2%Yb^{2+},0.5%Sm^{2+} and 85% for $CsBa_2I_5$:2%Yb^{2+},1%Sm^{2+} and $CsBa_2I_5$:5%Yb^{2+},1%Sm^{2+}.

Fig. 9b shows the photoluminescence decay time profiles of the Yb^{2+} spin-forbidden emission in $CsBa_2I_5$:Yb^{2+},Sm^{2+}. Similar to Fig. 9a, $CsBa_2I_5$:2%Yb^{2+} (curve 1) shows almost perfect exponential decay and the decay time profiles of the Sm^{2+} co-doped samples are non-exponential (curves 2, 3 and 4). This shows that radiationless energy transfer also takes place from the Yb^{2+} $4f^{13}[^2F_{7/2}]5d_1$[HS] state to Sm^{2+}. The concentration dependence is nearly identical and thereby the values of the radiationless energy transfer efficiencies are similar. In fact, the only striking difference is the factor of 300 longer timescale of Fig. 9b compared to Fig. 9a.

The photoluminescence decay of the Yb^{2+} emission in $CsBa_2I_5$:2% Yb^{2+} is shown in Fig. 10a for temperatures between 350 K and 550 K. Similar to Fig. 8, the fast component is the spin-allowed emission and the slow component is the spin-forbidden emission. When the temperature is increased from 350 K to 550 K, the spin-allowed emission quenches, as seen by rapid shortening of its decay time. Meanwhile, the intensity of the spin-forbidden emission increases.

Fig. 10b shows the photoluminescence decay of the Yb^{2+} emission in $CsBa_2I_5$:2%Yb^{2+},1%Sm^{2+}. Also here, the spin-allowed emission quenches and the intensity of the spin-forbidden emission increases as temperature is increased from 350 K to 550 K. Both the Yb^{2+} spin-allowed and spin-forbidden decay times are faster than for $CsBa_2I_5$:2% Yb^{2+} in Fig. 10a. This is due to radiationless energy transfer to Sm^{2+}.

Fig. 11a shows photoluminescence decay of the Sm^{2+} $4f^55d \rightarrow 4f^6$ emission in $CsBa_2I_5$:2%Yb^{2+},0.5%Sm^{2+} excited at 25,700 cm^{-1} between 350 K and 550 K. This energy corresponds to the spin-allowed $4f^{14} \rightarrow 4f^{13}[^2F_{7/2}]5d_1$[LS] excitation band of Yb^{2+}, meaning that both Yb^{2+} and Sm^{2+} are excited by the laser. The Sm^{2+} ions that are excited directly by the laser will contribute to the intensity of the decay time profile promptly after excitation, while the Sm^{2+} ions that are excited by energy transfer from Yb^{2+} have their contribution delayed. The Sm^{2+} $4f^55d \rightarrow 4f^6$ emission decay time profiles are normalised to their value at $t = 0$, keeping the intensity due to direct Sm^{2+} excitation constant. The emission intensity continues to increase in the first 50–200 ns after excitation. In this stage, more Sm^{2+} ions are excited by energy transfer from Yb^{2+} than are emitting. The size of this increase in intensity decreases as temperature is raised from 350 K to 550 K.

Fig. 11b shows the photoluminescence decay of the Sm^{2+} emission in $CsBa_2I_5$:2%Yb^{2+},1%Sm^{2+} between 350 K and 550 K, also excited at 25,700 cm^{-1}. All decay time profiles are normalised to their maximum. The decay time profiles have a slow component at every temperature.

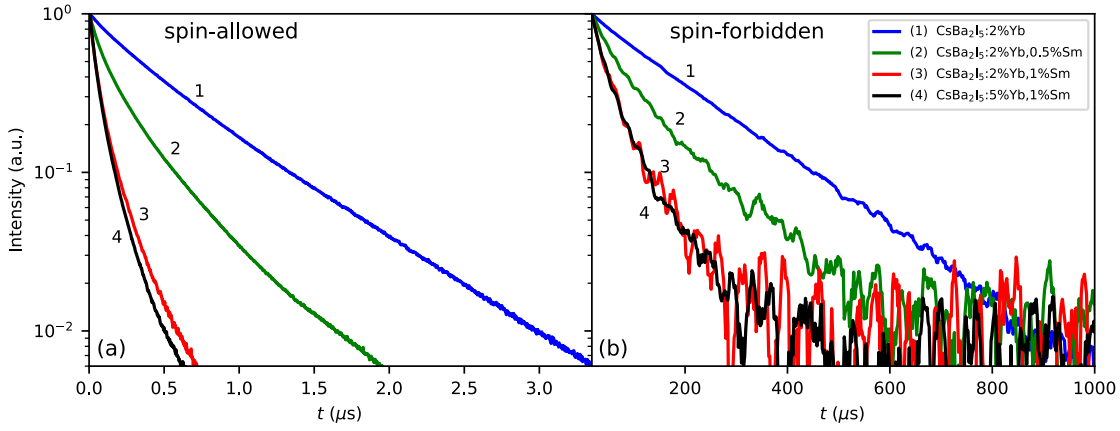

Fig. 9. Concentration dependent luminescence decay time profiles of Yb^{2+} emission in $CsBa_2I_5$:Yb^{2+},Sm^{2+} after excitation into the $4f^{13}[^2F_{7/2}]5d_1$[LS] state at room temperature. (a): Monitored at the maximum of the $4f^{13}[^2F_{7/2}]5d_1$[LS] → $4f^{14}$ emission at 24,000 cm^{-1}. The decay time profiles are normalised to their value at 0 μs. (b): Monitored at the maximum of the $4f^{13}[^2F_{7/2}]5d_1$[HS] → $4f^{14}$ emission at 22,400 cm^{-1}. The decay time profiles are normalised to their value at 18 μs, chosen as the optimal value to remove the $4f^{13}[^2F_{7/2}]5d_1$[LS] → $4f^{14}$ emission from the image while retaining an almost complete picture of the $4f^{13}[^2F_{7/2}]5d_1$[HS] → $4f^{14}$ decay.

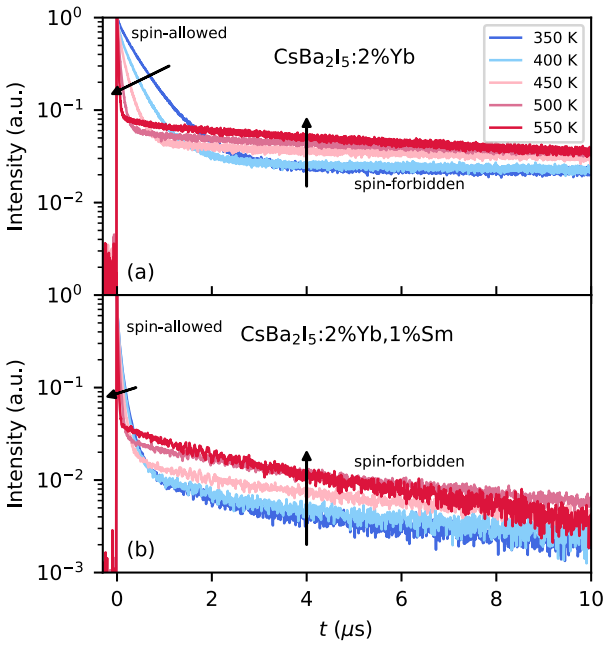

Fig. 10. Photoluminescence decay time profiles of the Yb^{2+} emission in (a) $CsBa_2I_5$:2%Yb^{2+} and (b) $CsBa_2I_5$:2%Yb^{2+},1%Sm^{2+}. Yb^{2+} is excited in the spin-allowed $4f^{14} \rightarrow 4f^{13}[^2F_{7/2}]5d_1$[LS] excitation band at 25,700 cm^{-1} and monitored at the peak of the spin-forbidden $4f^{13}[^2F_{7/2}]5d_1$[HS] $\rightarrow 4f^{14}$ emission at 22,400 cm^{-1} between 350 K and 550 K.

The intensity of this slow component increases as temperature is increased from 350 K to 550 K. This indicates that this slow component is caused by slow energy transfer from the $4f^{13}[^2F_{7/2}]5d_1$[HS] state of Yb^{2+}.

4. Discussion

4.1. Concentration dependent Yb^{2+} emission

Fig. 2a and b show that under X-ray excitation, the ratio of spin-forbidden to spin-allowed emission strongly increases with increasing Yb^{2+} concentration. The same increase in ratio between the spin-forbidden to spin-allowed emission has been observed in Yb^{2+}-doped $SrCl_2$ [23], Cs_4CaI_6 and Cs_4SrI_6 [24]. This phenomenon is also visible in Fig. 8, where the intensity of the slow component due to spin-forbidden emission is stronger in $CsBa_2I_5$:2%Yb^{2+} than in $CsBa_2I_5$:0.3%Yb^{2+}.

Sekine et al. proposed that self-absorption of the spin-allowed emission causes a concentration dependence of the ratio between spin-forbidden to spin-allowed emission [23]. In this process, spin-allowed emission is reabsorbed by the spin-allowed $4f^{14} \rightarrow 4f^{13}[^2F_{7/2}]5d_1$[LS] transition of another Yb^{2+} ion. From here, the newly excited Yb^{2+} ion can again decay radiatively, or relax non-radiatively to the $4f^{13}[^2F_{7/2}]5d_1$[HS] state from which spin-forbidden emission takes place. This self-absorption takes place at the energy where the spin-allowed excitation and spin-allowed absorption bands overlap. Due to the Stokes shift, this is on the high energy side of the spin-allowed emission, which decreases the probability of the spin-allowed emission photons with higher energy exiting the sample. This causes a red-shift of the spin-allowed emission band with increasing Yb^{2+} concentration, which has been observed in $SrCl_2$:Yb^{2+} [23]. This red-shift was not observed for the spin-forbidden emission, as the probability of absorption by the spin-forbidden transition is much lower than by the spin-allowed transition.

Self-absorption causes a photon to be reabsorbed and emitted again at a later time. This causes a lengthening of the observed photoluminescence decay time. The probability of self-absorption scales with the number of Yb^{2+} ions an emitted photon passes on its path leaving the sample, which in turn scales with the samples size and Yb^{2+} concentration [4]. This lengthening of the decay time has been observed in Cs_4CaI_6:Yb^{2+} for increasing crystal size while keeping the Yb^{2+} concentration constant [24]. However, Fig. 8 shows that as the Yb^{2+} concentration is increased, the spin-allowed decay time decreases and becomes slightly non-exponential. This indicates that self-absorption cannot be the only process that causes a concentration dependence of the ratio between spin-forbidden to spin-allowed emission.

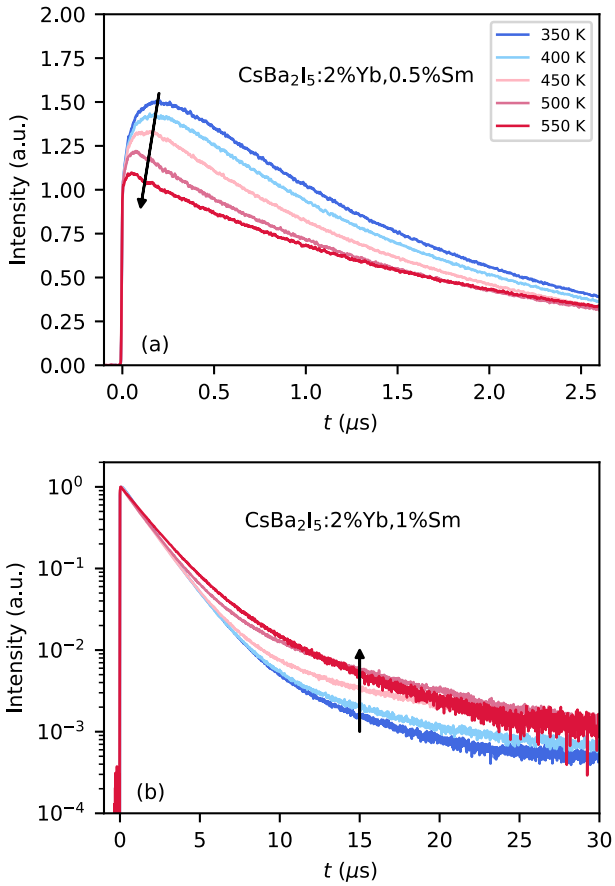

Fig. 11. Photoluminescence decay time profiles of Sm^{2+} emission excited at 25,700 cm^{-1} and monitored at 13,300 cm^{-1} between 350 K and 550 K. (a) $CsBa_2I_5$:2%Yb^{2+},0.5%Sm^{2+} showing a decrease in energy transfer from the Yb^{2+} $4f^{13}[^2F_{7/2}]5d_1$[LS] state. (b) $CsBa_2I_5$:2%Yb^{2+},1%Sm^{2+} showing an increase in energy transfer from the Yb^{2+} $4f^{13}[^2F_{7/2}]5d_1$[HS] state.

In Fig. 5 it is shown that the spin-allowed emission band and the spin-forbidden excitation band overlap at around 24,000 cm^{-1}. According to Förster-Dexter theory, this is the criterium for radiationless energy transfer from the $4f^{13}[^2F_{7/2}]5d_1$[LS] state to the $4f^{13}[^2F_{7/2}]5d_1$[HS] state of another Yb^{2+} ion. The probability of this process scales with the Yb^{2+} concentration. A schematic of this process is depicted in Fig. 12. The configurational coordinate diagram of a pair of Yb^{2+} ions is shown. Initially, ion 1 is in the $4f^{13}[^2F_{7/2}]5d_1$[LS] state and ion 2 is in the $4f^{14}$ ground state. Radiationless energy transfer from ions 1 to ion 2 is depicted by arrows A. The Stokes shift and exchange splitting have approximately the same value, resulting in arrow A having approximately equal length for ions 1 and 2. After radiationless energy transfer occured, lattice relaxation takes place around both ions (arrows B). The energy dissipated by lattice relaxation makes this process irreversible.

This process also explains the non-exponential decay of the spin-

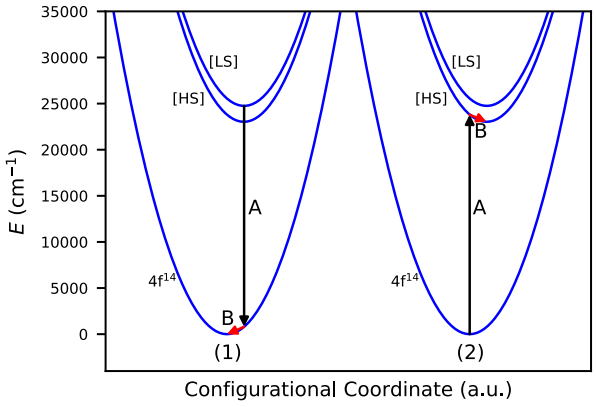

Fig. 12. Schematic of the energy transfer mechanism from the Yb^{2+} $4f^{13}[^2F_{7/2}]5d_1$[LS] to $4f^{13}[^2F_{7/2}]5d_1$[HS] state.

allowed emission in $CsBa_2I_5$:2%Yb^{2+} that is observed in Fig. 8. The Yb^{2+} $4f^{13}[^2F_{7/2}]5d_1$[LS] state acts as a donor state for the $4f^{13}[^2F_{7/2}]5d_1$[HS] state. The excited Yb^{2+} ions that have many other Yb^{2+} ions nearby have a larger probability of transferring their energy and will on average show a shorter excited state lifetime. With progress of time, the remaining Yb^{2+} ions still in the $4f^{13}[^2F_{7/2}]5d_1$[LS] state are the ones that have no Yb^{2+} ions nearby. This causes the lifetime to become progressively longer as more Yb^{2+} ions decay. The $4f^{13}[^2F_{7/2}]5d_1$[HS] state does not act as a donor state, making its decay time independent of concentration.

It is likely that both self-absorption and non-radiative energy transfer between Yb^{2+} ions play a role. Which of the two processes is more prominent depends on the Yb^{2+} concentration and sample size. Both processes change the spin-allowed photoluminescence decay time in opposite directions, but change the ratio between spin-forbidden to spin-allowed emission in the same direction. This allows for a large change in ratio between spin-forbidden and spin-allowed emission intensity while the change in decay time is relatively small.

Fig. 2c and d show that the spin-allowed emission quenches when the temperature is increased from 300 K to 450 K until eventually only spin-forbidden emission is left. Quenching of the spin-allowed emission is also observed in Fig. 10a. This process has been discussed in depth by Suta and Wickleder and is attributed to thermal relaxation from the Yb^{2+} $4f^{13}[^2F_{7/2}]5d_1$[LS] state to the $4f^{13}[^2F_{7/2}]5d_1$[HS] state [29]. Suta and Wickleder found that the temperature at which thermal relaxation becomes competitive with spin-allowed emission depends strongly on type of anion. For iodides this temperature has been observed between 400 K and 500 K [22,29], which is in agreement with the data presented in Figs. 2 and 10a.

In order to compete with some of the best Eu^{2+}-doped halide scintillators, a light yield of nearly 100,000 ph/MeV is required. This can only be achieved if the luminescence is virtually lossless. Most photons that originate from the spin-forbidden transition will take longer than the shaping time to arrive at the detector. This causes them to be discarded and should be considered lost for applactions in γ-ray spectroscopy. Therefore, the amount of spin-forbidden emission must be kept to a minimum, putting an upper limit on the Yb^{2+} concentration. The best performance of Eu^{2+}-doped halides is often found at Eu^{2+} concentrations between 5% and 10% [8,10,34], suggesting that similar Yb^{2+} concentrations would be required to attain optimal results. Therefore, the problem of increasing spin-forbidden emission intensity needs to be addressed to make Yb^{2+}-doped halides competitive with their Eu^{2+}-doped counterparts.

To minimise the spin-forbidden emission, the spin-allowed emission needs to compete more strongly with the relaxation processes from the Yb^{2+} $4f^{13}[^2F_{7/2}]5d_1$[LS] state to the $4f^{13}[^2F_{7/2}]5d_1$[HS] state. This would require careful selection of the proper host material. Thermal relaxation is minimised by choosing a host with low phonon frequencies [29], making iodides the most suitable within the family of halides. Relaxation through energy transfer from the $4f^{13}[^2F_{7/2}]5d_1$[LS] state to the $4f^{13}[^2F_{7/2}]5d_1$[HS] state can be reduced in several ways. One way is to reduce the overlap between the spin-allowed emission band and the spin-forbidden excitation band, i.e. the exchange splitting and Stokes shift need to have different values. Also, a low absorption strength of the Yb^{2+} $4f^{14} \rightarrow 4f^{13}[^2F_{7/2}]5d_1$[HS] excitation band reduces the rate of energy transfer. Lastly, the probability of radiationless energy transfer decreases rapidly with increasing distance between donor and acceptor, so hosts in which the distance between Yb^{2+} sites is relatively large are desired. Additionally, radiationless energy transfer from the Yb^{2+} $4f^{13}[^2F_{7/2}]5d_1$[LS] state to another emission center (e.g. Sm^{2+}) can be used to compete with the relaxation processes to the Yb^{2+} $4f^{13}[^2F_{7/2}]5d_1$[HS] state.

4.2. Yb^{2+} as a scintillation sensitiser for Sm^{2+}

Fig. 13 shows a schematic overview of the energy transfer from Yb^{2+} to Sm^{2+}. The scale of the VRBE scheme in Fig. 1 has been used. The relevant transitions are based on the results of this article and are further discussed below. The Yb^{2+} spin-allowed (arrow 1) and spin-forbidden emission (arrow 2) and the multiphonon relaxation from the Yb^{2+} $4f^{13}[^2F_{7/2}]5d_1$[LS] state to the $4f^{13}[^2F_{7/2}]5d_1$[HS] state (arrow 3) have been discussed in section 4.1.

In samples containing Sm^{2+}, energy transfer from Yb^{2+} to Sm^{2+} takes place. In Fig. 7 this is shown by the excitation bands of Yb^{2+} (curve 3)

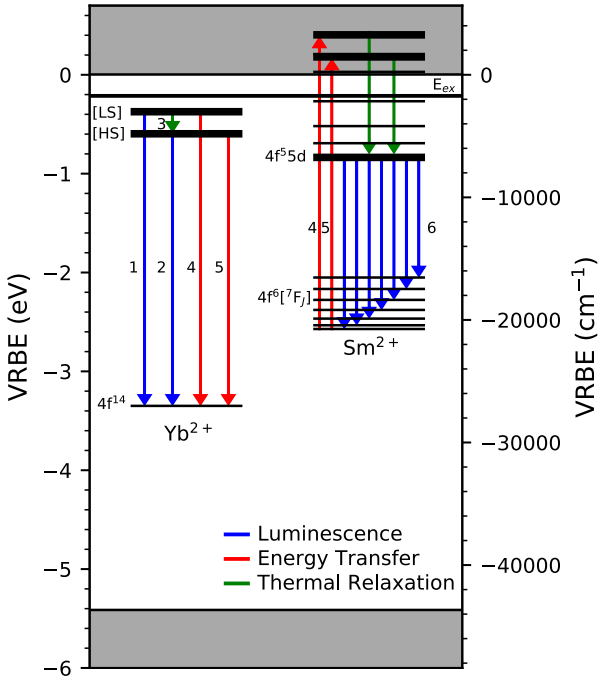

Fig. 13. Schematic overview of the energy transfer from Yb^{2+} to Sm^{2+}. The energy scale is identical to that of Fig. 1. The arrows indicate the transitions discussed in this work: (1) Yb^{2+} spin-allowed emission, (2) Yb^{2+} spin-forbidden emission, (3) Thermal relaxation from the Yb^{2+} $4f^{13}[^2F_{7/2}]5d_1$[LS] to $4f^{13}[^2F_{7/2}]5d_1$[HS] state, (4) Energy transfer from the Yb^{2+} $4f^{13}[^2F_{7/2}]5d_1$[LS] state to Sm^{2+}, (5) Energy transfer from the Yb^{2+} $4f^{13}[^2F_{7/2}]5d_1$[HS] state to Sm^{2+}, (6) Sm^{2+} $4f^5 5d \rightarrow 4f^6[^7F_J]$ emission.

being visible in the excitation spectrum of Sm^{2+} (curve 2). In Fig. 9 it is shown by the photoluminescence decay of Yb^{2+} becoming non-exponential for all samples containing Sm^{2+}. This happens for both the spin-allowed (Fig. 9a) and spin-forbidden (Fig. 9b) emissions, meaning radiationless energy transfer takes place from both the Yb^{2+} $4f^{13}[^2F_{7/2}]5d_1$[LS] and $4f^{13}[^2F_{7/2}]5d_1$[HS] states. Energy transfer from the $4f^{13}[^2F_{7/2}]5d_1$[LS] state to Sm^{2+} is depicted in Fig. 13 by arrows 4. Energy transfer from the $4f^{13}[^2F_{7/2}]5d_1$[HS] state is depicted by arrows 5.

The photoluminescence decay of the Yb^{2+} spin-allowed emission in Fig. 9a is approximately 300 times faster than the spin-forbidden emission in Fig. 9b. This is even the case for the samples containing Sm^{2+} where the Yb^{2+} decay is non-exponential, indicating not only luminescence, but also radiationless energy transfer to Sm^{2+} is 300 times faster from the $4f^{13}[^2F_{7/2}]5d_1$[LS] state than from the $4f^{13}[^2F_{7/2}]5d_1$[HS] state. This is predicted by Förster-Dexter theory, as the probability of energy transfer scales with the inverse of the intrinsic luminescence lifetime of the donor state τ_d (equation (1)).

Both Yb^{2+} donor states have approximately the same energy transfer efficiency. When co-doped with 1% Sm^{2+}, already about 85% of the Yb^{2+} excitations are transferred to Sm^{2+} through radiationless energy transfer. Fig. 3 shows that the $CsBa_2I_5$:Yb^{2+},Sm^{2+} samples show almost exclusively Sm^{2+} $4f^55d \rightarrow 4f^6[^7F_J]$ emission (arrows 6 in Fig. 13) under X-ray excitation. The combination of radiationless and radiative energy transfer results in almost complete transfer of energy from Yb^{2+} to Sm^{2+} at a Sm^{2+} concentration low enough to not cause significant self-absorption.

The lifetime of the Sm^{2+} $4f^55d$ state is 2.1 μs in $CsBa_2I_5$ [14], which is longer than the lifetime of the Yb^{2+} $4f^{13}[^2F_{7/2}]5d_1$[LS] state. Because of this, energy transfer from the Yb^{2+} $4f^{13}[^2F_{7/2}]5d_1$[LS] state to Sm^{2+} causes a contribution to the Sm^{2+} emission decay that has a rise time (Fig. 11a). As temperature is increased from 350 K to 550 K, the intensity of this contribution decreases. This happens at the same temperature as the Yb^{2+} spin-allowed emission quenches due to thermal relaxation in samples not containing Sm^{2+}, indicating that the contribution with rise time is caused by radiationless energy transfer from the Yb^{2+} $4f^{13}[^2F_{7/2}]5d_1$[LS] state to Sm^{2+}.

Radiationless energy transfer from the Yb^{2+} $4f^{13}[^2F_{7/2}]5d_1$[HS] state to Sm^{2+} is not fast enough to make the lifetime of the Yb^{2+} $4f^{13}[^2F_{7/2}]5d_1$[HS] state shorter than the lifetime of the Sm^{2+} $4f^55d$ state. This causes energy transfer from the Yb^{2+} $4f^{13}[^2F_{7/2}]5d_1$[HS] state to create a slow component in the Sm^{2+} emission (Fig. 11b). As temperature is increased from 350 K to 550 K, the intensity of the slow component increases. Thermal relaxation from the Yb^{2+} $4f^{13}[^2F_{7/2}]5d_1$[LS] to $4f^{13}[^2F_{7/2}]5d_1$[HS] state increases the amount of energy transferred to Sm^{2+} from the $4f^{13}[^2F_{7/2}]5d_1$[HS] state.

Table 2 shows an overview of the scintillation properties of $CsBa_2I_5$ with various dopants. All values were obtained using a shaping time of 10 μs. Most of the light emitted in the slow components of the Yb^{2+}-doped samples falls outside this shaping time and does therefore not contribute to the observed light yield, while this would be crucial for achieving an energy resolution below 2%. As a consequence, an energy resolution of 7.9% was attained with $CsBa_2I_5$:2%Yb^{2+},1%Sm^{2+}, as opposed to the energy resolution of 3.2% attained with $CsBa_2I_5$:2% Eu^{2+},1%Sm^{2+} [14]. Just like the Yb^{2+} spin-forbidden emission of $CsBa_2I_5$:Yb^{2+}, the slow component in the Sm^{2+} emission of $CsBa_2I_5$:Yb^{2+},Sm^{2+} originates from population of the Yb^{2+} $4f^{13}[^2F_{7/2}]5d_1$[HS] state. Therefore, solutions found for Yb^{2+}-doped scintillators will likely also be applicable to Sm^{2+} co-doped scintillators.

Table 2
Scintillation properties of $CsBa_2I_5$ samples. *R* denotes the energy resolution of the 662 keV photopeak and *Y* denotes the corresponding light yield.

Compound	*R* (%)	*Y* (ph/MeV)	Detector	Ref.
$CsBa_2I_5$:Eu^{2+}	2.3	100,000	PMT	[4,5]
$CsBa_2I_5$:2%Eu^{2+},1%Sm^{2+}	3.2	45,000	APD	[14]
$CsBa_2I_5$:0.3%Yb^{2+}	17.5	58,000	PMT	This work
$CsBa_2I_5$:2%Yb^{2+}	7.2	39,000	PMT	This work
$CsBa_2I_5$:2%Yb^{2+},1%Sm^{2+}	7.9	26,000	APD	This work

5. Conclusions

The feasibility of using Yb^{2+} as a scintillation sensitiser for $CsBa_2I_5$:Sm^{2+} near-infrared scintillators has been assessed. $CsBa_2I_5$:Yb^{2+} is found to show an increasing spin-forbidden to spin-allowed emission ratio as the Yb^{2+} concentration is increased. Radiationless energy transfer from the $4f^{13}[^2F_{7/2}]5d_1$[LS] state to the $4f^{13}[^2F_{7/2}]5d_1$[HS] state of another Yb^{2+} ion is found to play a significant role in this concentration dependent ratio. It is caused by the spin-allowed $4f^{13}[^2F_{7/2}]5d_1$[LS] → $4f^{14}$ emission band overlapping with the spin-forbidden $4f^{14}$ → $4f^{13}[^2F_{7/2}]5d_1$[HS] excitation band. The spin-forbidden emission is too slow for scintillator applications. This problem can be solved by selecting host materials in which these two bands have less overlap.

Photoluminescence decay time profiles of $CsBa_2I_5$:Yb^{2+},Sm^{2+} have revealed that the $4f^{13}[^2F_{7/2}]5d_1$[LS] and $4f^{13}[^2F_{7/2}]5d_1$[HS] states of Yb^{2+} both serve as donor states for Sm^{2+} emission. The rates of energy transfer are inversely proportional to the intrinsic luminescence lifetime of the respective excited states. This results in energy transfer from the Yb^{2+} $4f^{13}[^2F_{7/2}]5d_1$[HS] state to Sm^{2+} happening on a 100 μs–1000 μs timescale, causing a slow component in the Sm^{2+} $4f^55d \rightarrow 4f^6$ emission. This slow component is also too slow for scintillator applications. As the slow component is of the same origin as the spin-forbidden emission of Yb^{2+}, it is expected that improvements in Yb^{2+}-doped scintillators will also yield better results for their Sm^{2+} co-doped counterparts.

With only 1% Sm^{2+} co-doping, 85% of the excitations on Yb^{2+} are transferred to Sm^{2+} through radiationless energy transfer. Almost all remaining Yb^{2+} emission is reabsorbed by Sm^{2+} as well, resulting in almost 100% energy transfer. This shows that only a low concentration of Sm^{2+} is required to potentially arrive at a near-infrared scintillator with a light yield similar to those of Eu^{2+}-doped halides, while avoiding the self-absorption problem these scintillators face.

Author statement

Casper van Aarle was responsible for performing the experiments, writing the manuscript, preparing the figures and literature research. Karl W. Krämer was responsible for the materials and reviewing and editing the manuscript. Pieter Dorenbos was responsible for supervision of the project and reviewing and editing the manuscript.

Declaration of competing interest

The authors declare that they have no known competing financial interests or personal relationships that could have appeared to influence the work reported in this paper.

Acknowledgements

This research was subsidised by the TTW/OTP grant no. 18040 of the Dutch Research Council. The authors would like to thank Daniel Biner, Bern, for the synthesis and crystal growth of the materials.

References

[1] Pieter Dorenbos, Opt. Mater. X. 1 (2019) 100021.
[2] M.S. Alekhin, J.T.M. de Haas, I.V. Khodyuk, K.W. Krämer, P.R. Menge, V. Ouspenski, P. Dorenbos, Appl. Phys. Lett. 102 (2013) 161915.
[3] E.V.D. van Loef, P. Dorenbos, C.W.E. van Eijk, K. Krämer, H.U. Güdel, Appl. Phys. Lett. 79 (2001) 1573.
[4] Mikhail S. Alekhin, Karl W. Krämer, Pieter Dorenbos, J. Lumin. 714 (2013) 13.
[5] Gregory Bizarri, D. Edith, Bourret Courchesne, Zewu Yan, Steve E. Derenzo, IEEE Trans. Nucl. Sci. 58 (2011) 3403.
[6] R. Hawrami, J. Glodo, K.S. Shah, N. Cherepy, S. Payne, A. Burger, L. Boatner, J. Cryst. Growth 379 (2013) 63.
[7] M.J. Weber, Nucl. Instrum. Methods A. 527 (2004) 9.
[8] Jarek Glodo, Edgar V. van Loef, Nerine J. Cherepy, Stephen A. Payne, Kanai S. Shah, IEEE Trans. Nucl. Sci. 57 (2010) 1228.
[9] Yuntao Wu, Mariya Zhuravleva, Adam C. Lindsey, Merry Koschan, Charles L. Melcher, Nucl. Instrum. Methods A. 820 (2016) 132.
[10] Mikhail S. Alekhin, Daniel A. Biner, Karl W. Krämer, Pieter Dorenbos, J. Lumin. 145 (2014) 723.
[11] L. Stand, M. Zhuravleva, G. Camarda, A. Lindsey, J. Johnson, C. Hobbs, C. L. Melcher, J. Cryst. Growth 439 (2016) 93.
[12] R.H.P. Awater, M.S. Alekhin, D.A. Biner, K.W. Krämer, P. Dorenbos, J. Lumin. 212 (2019) 1.
[13] Johan T.M. de Haas, Pieter dorenbos, IEEE Trans. Nucl. Sci. 55 (2008) 1086.
[14] Weronika Wolszczak, Karl W. Krämer, Pieter Dorenbos, Phys. Status Solidi R. 13 (2019) 1900158.
[15] D.L. Dexter, J. Chem. Phys. 21 (1953) 836.
[16] Marvin J. Weber, Phys. Rev. B 4 (1971) 2932.
[17] R.G. Bennett, J. Chem. Phys. 41 (1964) 3037.
[18] Mitio Inokuti, Fumio Hirayama, J. Chem. Phys. 43 (1965) 1978.
[19] Eiichiro Nakazawa, J. Shigeo Shionoya, Chem. Phys. 47 (1967) 3211.
[20] R.D. Shannon, Acta Crystallogr. A. 32 (1976) 751.
[21] Emmanuel Rowe, Pijush Bhattacharya, Eugene Tupitsyn, Michael Groza, Arnold Burger, Nerine J. Cherepy, Steve A. Payne, Benjamin W. Sturm, C. Pédrini, IEEE Trans. Nucl. Sci. 60 (2013) 1057.
[22] Mikhail S. Alekhin, Daniel A. Biner, Karl W. Krämer, Pieter Dorenbos, Opt. Mater. 37 (2014) 382.
[23] Sekine Dai, Yutaka Fujimoto, Masanori Koshimizu, Daisuke Nakauchi, Takayuki Yanagida, Keisuke Asai, Jpn. J. Appl. Phys. 59 (2020), 012005.
[24] Daniel Rutstrom, Luis Stand, Bogdan Dryzhakov, Merry Koschan, L. Melcher Charles, Mariya Zhuravleva, Opt. Mater. 110 (2020) 110536.
[25] Markus Suta, Claudia Wickleder, J. Lumin. 210 (2019) 210.
[26] P. Dorenbos, J. Alloys Compd. 341 (2002) 156.
[27] Markus Suta, Tim Senden, Olchowka Jacob, Matthias Adlung, Andries Meijerink, Claudia Wickleder, Phys. Chem. Chem. Phys. 19 (2017) 7188.
[28] Taiju Tsuboi, Donald S. McClure, Wing C. Wong, Phys. Rev. B 48 (1993) 62.
[29] Markus Suta, Claudia Wickleder, Adv. Funct. Mater. 27 (2016) 1602783.
[30] P. Dorenbos, J. Phys. Condens. Matter 15 (2003) 575.
[31] Markus Suta, Urland Werner, Claude Daul, Claudia Wickleder, Phys. Chem. Chem. Phys. 18 (2016) 13196.
[32] S. Kück, M. Henke, K. Rademaker, Laser Phys. 11 (2001) 116.
[33] W. Wolszczak, K.W. Krämer, P. Dorenbos, J. Lumin. 222 (2020) 117101.
[34] Daniel Rutstrom, Luis Stand, Merry Koschan, Charles L. Melcher, Mariya Zhuravleva, J. Lumin. 216 (2019), 116740.
[35] Pieter Dorenbos, J. Lumin. 222 (2020), 117164.
[36] Pieter Dorenbos, J. Lumin. 135 (2013), 93.